High Efficiency Hybrid Solar Cells Using Nanocrystalline Si Quantum Dots and Si Nanowires

Mrinal Dutta,* Lavanya Thirugnanam, Pham Van Trinh, and Naoki Fukata*

International Center for Materials Nanoarchitectonics (MANA), National Institute for Materials Science, 1-1 Namiki, Tsukuba 305-0044, Japan

ABSTRACT We report on an efficient hybrid Si nanocrystal quantum dot modified radial p—n junction thinner Si solar cell that utilizes the advantages of effective exciton collection by energy transfer from nanocrystal-Si (nc-Si) quantum dots to underlying radial p—n junction Si nanowire arrays with excellent carrier separation and propagation *via* the built-in electric fields of radial p—n junctions. Minimization of recombination, optical, and spectrum losses in this hybrid structure led to a high cell efficiency of 12.9%.

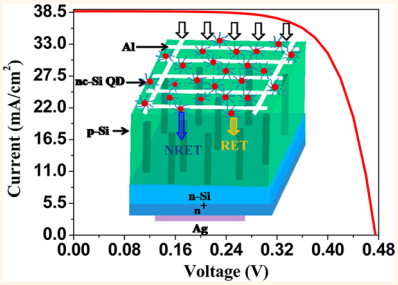

KEYWORDS: Si · solar cell · quantum dot · p—n junctions

Si solar cells with radial junction nanowire (NW) arrays offer the opportunity to use lower-grade Si wafers to produce efficient solar cells, due to the decoupling of charge carrier collection and light absorption directions with enhanced light trapping, thus resolving the drawbacks of bulk Si solar cells.[1,2] Despite the fact that spectral mismatch optical loss has been minimized to a great extent by efficient light trapping in SiNW-based solar cells, surface and bulk recombination losses play a dominant role in reducing efficiency.[3,4] To date, significant developments have been achieved in reducing the large surface and interface recombination of photogenerated charge carriers.[5—7] There remains, however, considerable room to reach experimental efficiencies that approach theoretical predictions.[8,9] Surface recombination in SiNWs has been minimized by surface/interface passivation, using an intrinsic layer at the interface, optimizing NW length, *etc.*[5,10—13] However, when minimizing surface recombination, it is also necessary to minimize bulk recombination, as SiNW arrays are synthesized on Si wafers. Thin wafer-based SiNW array solar cells are of interest as a low-cost replacement for thick wafer-based solar cells, due to the low cost of raw materials and high efficiency resulting from reduced bulk recombination.

Very recently, nonradiative energy transfer (NRET) has been proposed for hybrid nanostructures that combine absorbing components (*e.g.*, quantum dots) with high-mobility semiconducting channels. We predict this will open new possibilities in light harvesting.[14—21] Use of colloidal semiconductor nanocrystals in these hybrids provides the advantage of absorbing a wider range of the solar spectrum than Si layers are able to and exploiting the NRET process can overcome the limitations of low charge transfer efficiency in charge transfer-based devices. Long-range dipole—dipole interaction in NRET hybrids can exceed both short-range charge transfer and radiative energy transfer.[15—17] The experimental evidence has been observed in hybrid semiconductor heterostructures under optical excitation between a single semiconductor nanostructure and an adjacent layer of organic molecules[22,23] or colloidal CdS, CdSe and PbS quantum dots.[14—21] As concerns toxicity, Si nanocrystal quantum dots (nc-Si QDs)[24—27] offer a promising alternative to the heavy metal-containing compound semiconductor quantum dots currently used in studying NRET hybrids. Silicon nanocrystals (diameter <5 nm), due to the

* Address correspondence to sspmd.iacs@gmail.com; FUKATA.Naoki@nims.go.jp.

Received for review January 23, 2015 and accepted July 13, 2015.

Published online July 13, 2015
10.1021/acsnano.5b03268

confinement effect and depending on their encapsulating ligands, are able to emit in visible frequencies after absorbing the solar spectrum.[28−33]

In this report, we describe a new energy transfer (ET)-mediated 12.9%-efficient all-Si solar cell structure that overcomes surface and bulk recombination problems by means of good front contact patterning that reduces series resistance. n-type (100) Si substrates of thickness 170 μm with a resistivity of 27 $\Omega\cdot$cm have been used to realize high-efficiency radial p−n junction solar cells with minimal photogenerated charge carrier loss. Realization of the contributions from NRET and radiative energy transfer (RET) from nc-Si QDs to the Si layer was demonstrated by time-resolved photoluminescence decay measurements. The main advantage of this hybrid cell structure is the propagation of electron−holes, generated by the ET process beneath the Si layer, in the correct direction due to the presence of built-in electric fields of p−n junctions under zero bias. Our ET-mediated radial p−n junction solar cell structure offers the following advantages: (1) very low series resistance due to low contact resistance as a result of continuous front contact fabrication; (2) reduction of optical and recombination loss due to efficient light trapping with minimal surface and bulk recombination; (3) reduction of spectrum loss by greater solar light absorption cross section due to the absorption of the UV region of the solar spectrum by using Si nanocrystal quantum dots; (4) resonant excitation transfer from nc-Si QDs to the adjacent Si layer accompanied by the spontaneous creation of electrons and holes; and (5) efficient electron and hole separation in p−n junctions and transport in oppositely doped high mobility Si channels, exploiting the advantages of radial p−n junctions and thus overcoming the bottleneck of exciton separation and transport in excitonic solar cells. However, to our knowledge, no experimental investigations of the solar cell properties of this type of hybrid structures utilizing nontoxic nc-Si QDs have as yet been reported that show the potential of the NRET process in enhancing solar cell conversion efficiency.

EXPERIMENTAL RESULTS AND DISCUSSION

The SiNW arrays were fabricated by metal-catalyzed electroless etching using n-type (100) Si substrates. The process of Si nanowire array solar cell fabrication as reported in our previous reports[11−13] and colloidal nc-Si QDs synthesis following the synthesis method reported by Veinot *et al.*[24,28−30,32,33] is detailed in Methods. The formation of a p-type Si shell layer was performed by CVD. nc-Si QDs were then spin-coated onto the top layer of cells at a spinning rate of 500 rpm using a nc-Si QD solution of 5 mg/mL (Figure 1a). Raman scattering measurements were performed to investigate the crystallinity of the Si wires, nc-Si QDs and the doping of B acceptor atoms at room temperature,

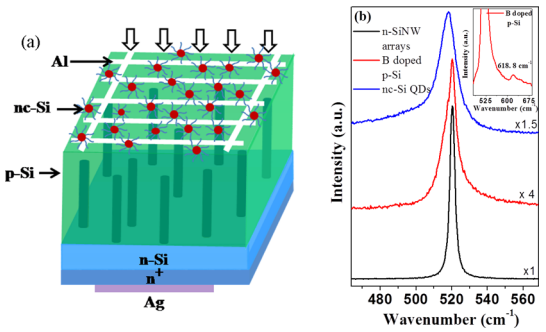

Figure 1. (a) Schematic diagram of the hybrid n-Si NW arrays embedded in a p-Si matrix solar cell. (b) Raman spectra of n-SiNW arrys, B doped p-Si top layer, and nc-Si QDs without capping. Inset shows magnification of the B local vibrational peak of the p-Si layer with smoothing.

as shown in Figure 1b. The Raman spectra observed for the n-SiNW arrays fabricated on the n-Si (100) substrates by MCEE technique showed a symmetric Si optical phonon peak, whereas the Si optical phonon peak in the B-doped p-Si layer shows an asymmetric broadening toward the higher wavenumber side,[34−36] due to the Fano effect caused by coupling between discrete optical phonons and the continuum of interband hole excitations in degenerately doped p-type Si.[37] In addition to the Si optical phonon peak, a B local vibrational peak was observed at around 618.8 cm^{-1}, which is in good agreement with the local vibrational peak in B-doped SiNWs.[29,38,39] Raman spectra of the uncapped nc-Si QDs shows a broadening toward the lower wavenumber side. This is due to the phonon confinement effect that results from their small size.[40−42]

HRTEM images of 1-octadecene capped nc-Si QDs (Figure 2a) show nearly spherical particles with a measured average diameter of 3.7 nm. Inset of Figure 2a shows high-resolution image of interplanar spacings of a representative nc-Si QD. The crystal fringes show a lattice interplanar spacing of 0.31 nm, corresponding to the *d* spacing of (111) crystal plane of diamond cubic structure of silicon. Energy dispersive X-ray (EDX) spectroscopy was carried out to confirm the elemental composition of the nc-Si QDs (Supporting Information Figure S3), demonstrating that samples consist of Si. However, no traces of O element was detected because this is due to very low O and below the detection limit in EDX measurement. The surface chemistry and surface passivation of the nc-Si QDs was verified by a Fourier transform infrared (FT-IR) spectroscopy as shown in Figure 2b. The FTIR spectrum shows the presence of characteristic C−H stretching (2850, 2917, and 2954 cm^{-1}) and bending (1377, 1466 cm^{-1}) attributed to the surface bonded alkyl groups.[27,43,44] A wide peak around 1052 cm^{-1} corresponding to Si−O−Si vibrations occurred due to the limited nanocrystal surface oxidation or reaction of EtOH with residual Si−H groups during purification.[31] The small

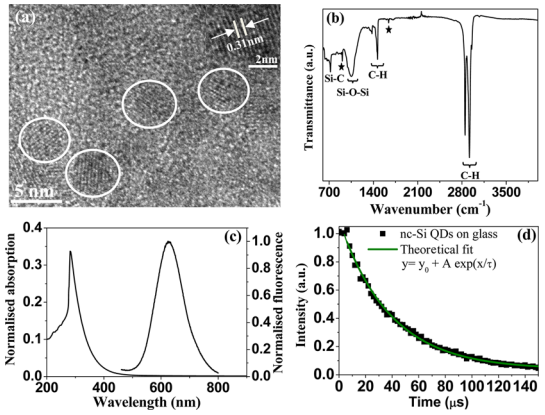

Figure 2. (a) Representative HRTEM images of 1-octadecence capped nc-Si QDs. Inset shows the inter planar (111) lattice plane of one of the diamond structured nc-Si QD. (b) FT-IR spectrum of the nc-Si QDs after hydrosilylation showing the presence of characteristic vibrations for surface terminating alkyl groups, little surface oxidation and small amount of residual 1-octadecene (★). (c) Absorption and fluorescence spectrum and (d) photoluminescence decay curve (λ_{ex} = 310 nm, embedded measured at the emission maximum) of the nc-Si QDs on glass.

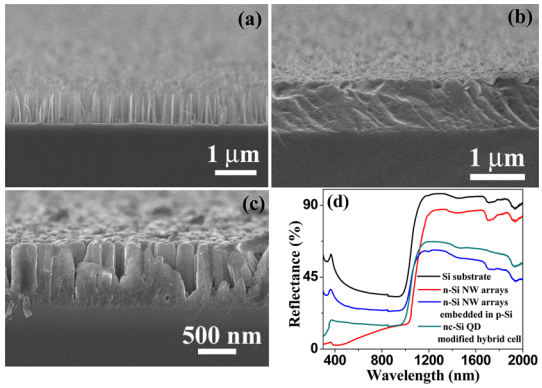

Figure 3. (a) Cross-sectional SEM image of the metal catalyzed electroless etched Si NW arrays. (b and c) Corresponding structures after 5 and 3 min of shell growth, respectively. (d) UV−vis reflection spectra of typical, planar Si (100) wafer, 700 nm-long Si NW arrays, n-Si NW arrays embedded in p-Si matrix structure, and nc-Si QD modified hybrid cell.

peaks at 908 and 1640 cm^{-1} are attributed to residual 1-octadecene.[31] The appearance of a small peak around 720 cm^{-1} may correspond to Si−C bond.[43] No observation of Si−H peaks in the FTIR spectra of Si QDs capped with 1-octadecene is due to the proper surface passivation. This observation is similar to the previous reports.[27,43] However, improper passivation sometimes gives rise to Si−H peaks in the FTIR spectra. In a recent report by Rieger and Veinot *et al.* [44] showed the presence of Si−H related peaks in the FTIR spectra of Si nanocrystals passivated with organolithium reagents. On the other hand, in a previous article, Veinot *et al.*[45] did not observe any prominent Si−H related peaks in the FTIR spectra of Si nanoparticles stabilized with trioctylphosphine oxide (TOPO).

The absorption and fluorescence spectrum of these QDs is shown in Figure 2c. The absorption spectrum shows an onset at 550 nm and a rising absorption edge into the UV. As seen in the fluorescence spectrum, an emission peak appears at around 627 nm with a full width at half-maximum of about 139 nm when excited with 284 nm light and a large Stokes shift of 343 nm. This large Stokes shift is the characteristic difference between nc-Si QDs and nc-QDs of compound semiconductors. The absolute quantum yield of the nc-Si QDs in toluene solution obtained by hydrosilylation of 1-octadecene was measured to be ∼30% which is comparable with previous reports.[46,47] Time dependent photoluminescence decay of the colloidal nc-Si QDs on a glass substrate was measured to explore the e−h carrier recombination dynamics in the ncSi-QD at room temperature (Figure 2d). The experimental decay plotted by small closed square boxes can be well fitted by single exponential decay curve with time constant of 29.24 μs. Both the large Stokes shift and slow photoluminescence decay are the characteristics of indirect band structure inherited even in quantum structures. However, the high quantum yield of the nc-Si QDs arises a complicated debate on the fluorescence origin of these nc-Si QDs.[48−50]

Cross-sectional scanning electron microscopic measurements were performed to characterize the surface structure of the SiNW arrays and solar cells. Figure 3a,b shows 5°-tilted cross-sectional SEM images of the SiNW arrays with an average length of 700 nm and the corresponding solar cell structure after CVD growth of the polycrystalline p-Si shell layer. The growth conditions were controlled in such way so that the shells touched each other to produce radial junction n-SiNW arrays embedded in the p-Si matrix solar cell structure. The advantage of this structure is that it facilitates good quality continuous front-contact fabrication. This is evidenced by the lower series resistance than those seen with core−shell NW structures (Figure 3c), as the series resistance is proportional to the contact resistance while maintaining all the parameters same for electrode fabrication [for details, see ref 11]. To obtain high efficiency, minimization of four fundamental losses need to be addressed: (1) optical; (2) recombination; (3) series resistance; and (4) thermal or spectrum loss. Figure 3d shows the reflectance spectra of a planar Si wafer with a polished surface, 700 nm-long SiNW arrays, SiNW arrays embedded in p-Si matrix structure, and nc-Si QDs modified hybrid cell structure over a broad spectral range from 220 to 2000 nm. The sharp transition around 1000−1150 nm in the reflectance spectrum corresponds to the band edge of Si.[51] Due to the subwavelength light trapping and collective light scattering interactions among the densely packed SiNWs, the average reflectance of SiNW arrays is suppressed to less than 7.5% in the 400−800 nm range compared to an average 38% reflection from planar Si wafer, while after shell growth,

the average reflection increases to ~26%.[12,13] In addition to this, the average reflectance of the hybrid cell substantially decreases to 16% after spin coating, indicating strong absorption by nc-Si QDs. In the longer-wavelength region (λ > 1150 nm), reflection reduces after shell growth compared to SiNW arrays. Earlier studies showed that excess free carriers facilitate phonon-assisted photon absorption in the near IR region.[52,53] Compared to n-type SiNW arrays, excess free carrier absorption in B doped shell layers increases photon absorption in the near-IR regions.[12] These increments of light trapping ensure reduction of optical losses in SiNW array solar cells without using any additional antireflection coating. Another dominating loss responsible for cell performance degradation is the surface and bulk recombination loss. The first is a bottleneck in SiNW solar cells and has drawn the attention of researchers worldwide. We addressed this question in our previous work, and the optimal length for SiNWs was obtained as approximately 700 nm for creating a bridge between optical loss and surface recombination loss.[11] Besides surface recombination, bulk recombination also degrades cell performance, though it has so far been paid little attention in SiNW array solar cells. Volume reduction by reducing the thickness of the wafer reduces the recombination rate, as described by the relationship[54]

$$R/V = n^{e}n^{h}v\sigma \quad (1)$$

where R is total recombination, V is the volume, n^{e} and n^{h} are the electron and hole density, v is average velocity, and σ is scattering cross section. The relationship of cell performance to bulk and surface recombination effects can be described by the effective minority carrier lifetime τ_{eff}, defined by[55]

$$1/\tau_{eff} = 1/\tau_{bulk} + (S^{F}{}_{eff} + S^{B}{}_{eff})/d \quad (2)$$

where τ_{bulk} is the bulk Shockley-Read-Hall lifetime, $S^{F}{}_{eff}$ and $S^{B}{}_{eff}$ are the effective surface recombination velocities at the cell front and back surfaces, and d is the cell thickness. Thus, from this equation, it is clear that as wafer thickness decreases, surface recombination tends to predominate over bulk recombination in determining the effective lifetime, which limits thinning of the cell wafer to 100−150 μm, as proposed by Mishima *et al.*[56] Figure 4a shows the thickness dependence of cell parameters normalized with respect to a 725 μm-thick wafer-based radial-junction SiNW array solar cell structure, as discussed above. For a 725 μm-thick wafer, huge bulk recombination results in very low fill factor. With decreasing thickness of the wafer, all cell parameters, such as short circuit current density (J_{sc}), open circuit voltage (V_{oc}), and fill factor (FF) improved by reflecting the reduction in bulk recombination loss. Creation of a back surface field at the rear surface of these thinner solar cells further enhances the

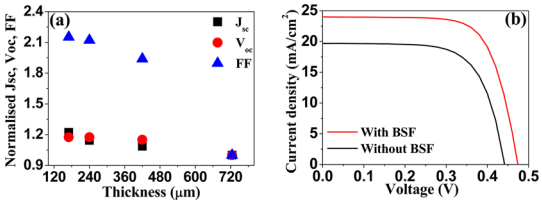

Figure 4. (a) Thickness dependence of solar cell parameters normalized with respect to a 725 μm-thick SiNW array solar cell and (b) current−voltage characteristic under 100 mW/cm^2 illumination with an AM 1.5 G solar simulator, showing the effect of the back surface field (BSF) in enhancing solar cell properties.

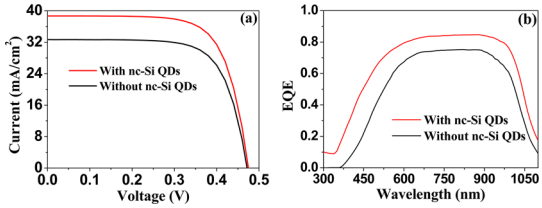

Figure 5. (a) Comparison of current−voltage characteristics of the best cells with and without nc-Si QDs of efficiency 12.9% and 10.9%, respectively, under simulated AM 1.5G illumination and (b) EQE of typical Si NW array of solar cells with and without nc-Si QDs.

conversion efficiency (η) by 36−45%. Figure 4b shows typical current−voltage (I−V) characteristics under 100 mW/cm^2 illumination to reflect the effect of the back surface field. V_{oc}, J_{sc}, and FF for solar cells with a back surface field increases from 0.44 to 0.47 V, 19.7 to 24.01 mA/cm^2, and 0.68 to 0.71, respectively, with an overall increase in efficiency from 5.9% to 8.1%. Furthermore, low temperature UV−ozone treatments effectively passivated surface recombination centers and improved the conversion efficiency by 20−25%. The effect of such UV−ozone treatment in passivating the surface/interface dangling bonds has been discussed in detail in our previous work.[11]

Figure 5a shows the I−V characteristic curves for the hybrid nc-Si QDs modified radial p−n junction thinner Si solar cell under 100 mW/cm^2 illumination by an AM 1.5G solar simulator in comparison with that of the solar cell without QDs. The solar cell with 700 nm long SiNW array fabricated on 170 μm thick wafer produces an average power conversion efficiency 10.3 ± 0.6% (V_{oc} of 0.46 ± 0.01, J_{sc} of 32.1 ± 0.6, and FF of 0.7 ± 0.01) (Table 1), and a maximum power conversion efficiency of 10.9%. On the other hand, the J_{sc} for the hybrid cell increased by 18.5% with an overall average power conversion efficiency improvement up to 12.2 ± 0.7% (Table 1) and a maximum of 12.9%, indicating the contribution arising from the presence of nc-Si QDs. In contrast to recent single-junction nanostructured solar cells, this hybrid cell shows significantly higher performance.[57−59] This improvement is also supported by the external quantum efficiency (EQE) measurements as shown in Figure 5b. Compared to only radial p−n junction thinner Si solar cell without modified by

TABLE 1. Average Photovoltaic Properties of nc-Si QDs Modified and Unmodified Thinner Si NW Array Solar Cells

sample	V_{oc} (V)	J_{sc} (mA/cm^2)	FF	η (%)
nc-Si QD modified hybrid cell	0.46 ± 0.01	38 ± 0.7	0.7 ± 0.01	12.2 ± 0.7
Without QD modified cell	0.46 ± 0.01	32.1 ± 0.6	0.7 ± 0.01	10.3 ± 0.6

nc-Si QDs, the hybrid solar cell modified with nc-Si QDs exhibits enhanced EQE from the UV to the near-IR region. This enhancement of EQE can be explained by the fact that energy transfer from nc-Si QDs to the underlying layer of solar cell creates further much more charge carriers and they also take part in conduction process.

nc-Si QDs deposited by spin coating on the top of poly p-Si layer transfer energy to the Si layers beneath both radiatively and nonradiatively. Charge transfer is facilitated by the electronic wave functions overlap with exponential dependence on the distance in angstrom-size scale. Therefore, the probability of charge transfer in the hybrid solar cell from the nc-Si QDs to the Si layer beneath can be ignored, since the nc-Si QDs are well covered by insulating ligands ~2 nm in length and separated by a 1−2 nm-thick SiO_2 layer from the Si layer beneath. Time dependent photoluminescence decays of the colloidal nc-Si QDs on the p-Si layer of the hybrid radial p−n junction thinner Si solar cell were measured and compared with those of nc-Si QDs on a glass substrate to characterize the efficiencies of radiative and nonradiative energy transfers in the hybrid structure. Comparison of the two photoluminescence decay curves clearly revealed the presence of an extra energy transfer channel in the hybrid structure, as shown in Figure 6. The single and bi exponential fits of the photoluminescence decays yield respective photoluminescence lifetime of nc-Si QDs on glass as τ_{glass} = 29.24 μs, and on p-Si layer τ_{hybrid} = 6.27 μs (for the fast component of the decay) and 27.58 μs (for the slow component of the decay). The close similarity in slow components of the photoluminescence decays suggests that interdot transfer mechanisms remain the same in the hybrid structure. The photoluminescence decay of nc-Si QDs on the glass substrate is dominated by the radiative and intrinsic nonradiative recombination channels (if any). However, in the hybrid structure, nonradiative energy transfer along with radiative energy transfer to the p-Si layer contributes to the nc-Si QDs photoluminescence decay rate as an extra energy transfer channel. This difference in photoluminescence decay lifetime compared to QDs on glass can therefore be attributed to the difference in radiative and nonradiative decay rates. Nonradiative decay strongly varies as $1/d^4$ according to the distance (d) from the Si surface and also as a function of the magnitude of the imaginary part of the complex dielectric function of Si.[15,60] For the decay of nc-Si QDs on glass, where photon emission is the main decay mechanism,[14] we

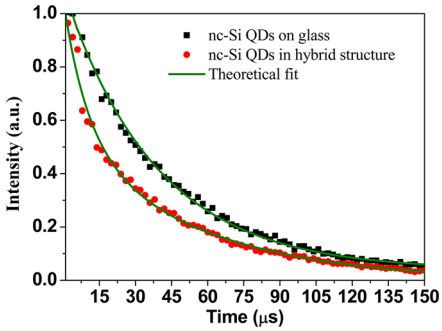

Figure 6. Time-resolved PL of nc-Si QDs on glass and in the hybrid structure at room temperature, at a detection wavelength of 625 nm.

can write $(\tau_{rad})^{-1} = QE\,(\tau_{tot})^{-1}$ where QE is the quantum yield and $(\tau_{tot})^{-1} = (29.24\ \mu s)^{-1}$ is the total decay rate. Here, the QE being ~30%, the radiative decay rate can be estimated as $\sim (97.5\ \mu s)^{-1}$. Thus, the decay rate of the QDs in the hybrid structure can be written as

$$(\tau_{hybrid})^{-1} = (\tau_{tot})^{-1} + (\tau_{ET})^{-1} \quad (3)$$

where $(\tau_{ET})^{-1}$ is the additional decay channel due to the energy transfer from QDs to the Si layer beneath. Thus, we can write

$$(\tau_{ET})^{-1} = (\tau_{RET})^{-1} + (\tau_{NRET})^{-1} \quad (4)$$

while the average distance of the QDs from the Si surface is estimated as ~5.5 nm. In this regime, the above equation can be written as

$$(\tau_{ET})^{-1} = QE(\tau_{hybrid})^{-1} + (\tau_{NRET})^{-1} \quad (5)$$

[assuming that the QE of the QDs is nearly same in the hybrid structure as that in toluene solution]. Thus, $(\tau_{RET})^{-1}$ and $(\tau_{NRET})^{-1}$ can be estimated as $\sim (20.9\ \mu s)^{-1}$ and $(12.9\ \mu s)^{-1}$, respectively. The nonradiative energy transfer rate is therefore ~1.6 times faster than radiative energy transfer rate to the underlying Si layer. Utilizing the well-known Forster equation relating the Forster transfer rate $(\tau_F)^{-1}$ with radiative decay rate as

$$(\tau_F)^{-1} = (R_0/r)^n(\tau_{rad})^{-1}$$

where n = 4 as predicted by the SDK theory[60] for the energy transfer from an excited molecule to the underlying semiconductor and using a nonradiative transfer rate of $(12.9\ \mu s)^{-1}$ and radiative transfer rate of $(20.9\ \mu s)^{-1}$, and the average distance between p-Si layer surface to QD center distance $r \sim 5.5$ nm, the Forster radius R_0 in this hybrid structure can be estimated to be ~6.2 nm.

Hence, our data shows the possibility of nonradiative energy transfer from nc-Si QDs. As already described in the introduction, NRET has been proposed between a single semiconductor nanostructure and an adjacent layer of organic molecules[22,23] or colloidal CdS, CdSe and PbS QDs.[14−21] However, no experimental results have been reported for nc-Si QDs. On the other hand, the NRET between nc-Si QDs has been discussed theoretically, showing that NRET is possible, but only when the two nc-Si QDs are almost in contact.[17] The nc-Si QDs and SiNWs used in this study are covered with ligands and native SiO_2 layers, respectively. The distance between the surface of nc-Si QDs and SiNWs corresponds to the sum of the ligands' length and the thickness of native SiO_2 layers, estimated to be about 4 nm. This distance is slightly greater than the theoretically estimated values at which NRET can occur in nc-Si.[17] The charge transfer from nc-Si QDs is more difficult to consider due to the presence of the ligands and native SiO_2 layers. On the basis of these results, NRET is one of the most likely reasons for increased short circuit current, and ultimately the increase in the energy conversion efficiency at the present time.

Finally, we discuss about the size of nc-SiQDs. Veinot *et al.*[28] earlier reported that the nc-Si QD core is more reduced by the continuation of HF etching of the nc-Si QDs/SiO_2 composite, resulting in the blue shift of emission while their absorption remain in UV region. On the other hand, modification of the silicon surface by hydrosilylation causes a shift (red/blue) of the emission peak depending on the emission wavelength of the etched Si nanocrystals. Gupta *et al.*[61] reported that red to orange luminescent etched Si nanoparticles show a blue-shift in the spectrum after hydrosilylation in contrast to green to yellow luminescent nanoparticles. The origin of this kind of opposite shift in emission after surface passivation remains unclear.[61,62] The absorption of nc-Si QDs in UV region and the opposite shift of the emission after surface passivation may restrict the advantage of use of different size QDs in further enhancing the efficiency of the NRET and RET based hybrid Si solar cells. Recently, Veinot *et al.*[32] reported that emission from the nc-Si QDs can be tuned from blue to red by chlorination, bromination, and iodination of hydride-terminated nc-Si QDs. Dhanolova *et al.*[63] also showed that carbon surface termination of the Si QDs alters indirect band gap into direct band gap like character through drastic modification in electron and hole wave functions and radiative transitions between the lowest excited states of electron and hole. All these research results widen the opportunity and potential to use the nc-Si QDs of different sizes with different emission and absorption wavelengths in Si solar photovoltaic to raise the efficiency further by funneling energy from nc-Si QDs to solar cells. Hence, energy transfer gives a new way to use nc-Si passivated with long chain alkyl groups which form an electrically insulating barrier that limits the performance of various semiconductor QDs devices.[64,65]

CONCLUSION

We report here nc-Si QDs integrated high efficiency n-SiNW arrays embedded in p-Si matrix structured thinner solar cells. This photon-harvesting architecture brings together the advantages of effective exciton collection by funneling energy from nc-Si QDs to SiNW arrays *via* energy transfer mechanisms, an approach with considerable potential, combined with excellent carrier separation and propagation due to the built-in electric fields of radial p−n junctions. Energy transfer mechanisms were demonstrated by time-dependent fluorescence decay measurements. The use of thin Si wafers with optimized length of SiNW arrays also reduced both bulk and surface recombination. Optical and spectrum losses were minimized by the use of SiNW array light trapping management and nc-Si QDs, respectively. Use of this architecture facilitates the continuous fabrication of front contacts, resulting in a reduction of series resistance.

METHODS

Reagents. Hydrogen silsesquioxane (HSQ) was purchased from Dow Chemical and used as received. Electronic-grade hydrofluoric acid (46% aqueous solution), nitric acid (HNO_3), sulfuric acid (H_2SO_4), hydrogen peroxide (H_2O_2), HPLC-grade toluene, ethanol, methanol, mesitylene, synthesis-grade $AgNO_3$, and 1-octadecene (Sigma-Aldrich) were used as received.

Fabrication Process of Si NW Arrays. SiNW arrays were prepared by metal-catalyzed electroless etching (MCEE) on n-type (100) single side polished Si substrates with resistivity of 27 Ω·cm. The Si substrates were cleaned with acetone (10 min) and ethanol (10 min) by sonication, then rinsed with deionized water 2−3 times and immersed in a 3:1 mixture of H_2SO_4 (96%) and H_2O_2 (30%) for 15 min. After thoroughly rinsing with deionized water 3−4 times, the Si substrates were dipped in 2% HF solution for 4 min. They were then immediately transferred to a Teflon beaker containing a solution of 0.02 M $AgNO_3$ in HF (4.6 M) to form vertically aligned Si NW arrays. The substrates were then rinsed thoroughly with deionized water. The etched Si substrates were finally immersed in concentrated HNO_3 (60%) for 6 min to remove Ag dendrites which had been deposited during etching.

Fabrication of Si NW Array Solar Cells. After the removal of the deposited Ag, the etched substrates were immersed in a HF (2%)/2-propanol solution for 8 min to remove the oxide layers on the SiNW surfaces. After rinsing with deionized water, the substrates were immediately placed on a holder in the CVD chamber to undergo deposition of the B doped p-type Si shell layers. The total pressure was set at around 8 Torr by mixing with N_2 gas (30 sccm). For B doping, 0.5 sccm of diborane (B_2H_6) gas was injected into the CVD chamber with 19 sccm of silane (SiH_4) gas during growth at 750 °C for 3 and 5 min. After forming the shell layers, rapid thermal annealing was performed at 950 °C for 3 min in an N_2 environment to activate the dopants.

The back surface field was created by spin coating of phosphorus-containing solution (OCD P-59210) and simultaneously prebaked at 450 °C for 30 min and annealed at 850 °C for 45 min in N_2 flow. UV−ozone treatments were done under 20 μW UV irradiation and 10 mTorr O_2 pressure at a temperature of 300 °C for 20 min. Solar cells were designed by depositing the Al front electrode (200 nm) in a finger grid pattern and the Ag (200 nm) back electrode by sputtering at room temperature.

Bulk nc-Si/SiO_2 Composite Preparation. Solvent was removed from the HSQ stock solution using a rotary evaporator heated in a water bath at 40 °C. The gel that formed was dried overnight under vacuum. The resulting white solid was placed in a quartz crucible and transferred in an inert atmosphere to a high-temperature furnace, where it was annealed at 1100 °C for 1 h in a 5% H_2 and 95% Ar atmosphere. The final temperature of 1100 °C was reached at a rate of 10 °C/min. After cooling to room temperature, the resulting dark brown solid was mechanically ground in a mortar and pestle to yield a fine powder.

Synthesis of Colloidal nc-Si QDs. A total of 200 mg of the fine powder was added to a mixture of 4 mL of ethanol, 4 mL of HF (46%), and 4 mL of milli-Q water and the solution stirred for 45 min to achieve the acidic etching of the SiO_2 matrix and a gradual decrease in size of core Si. After decanting most of the excess HF, hydride-terminated nanocrystalline Si quantum dots (nc-Si QDs) were centrifuged at 10 000 rpm with excess ethanol 2−3 times to remove any unreacted HF. After centrifugation, the product was dried under a dry N_2 flow to obtain ~20 mg of powder and transferred to a round-bottom flask containing 5 mL of mesitylene and 5 mL of 1-octadecene. This mixture was degassed for at least 1 h by Ar bubbling. Hydrosilylation of 1-octadecene on the surface of hydrogen-terminated nc-Si QDs was then carried out at 145 °C overnight in Ar ambient. After the reaction, the resulting transparent pale yellow solution was centrifuged with a small quantity of methanol to remove the mesitylene, and again centrifuged with toluene and methanol to remove the excess 1-octadecene. After centrifugation, 4 mL of toluene was added to obtain 1-octadecene capped hydrogen-terminated nc-Si QDs solution with a concentration of ~5 mg/mL.

Fabrication of nc-Si QD Decorated Si NW Array Hybrid Solar Cell. This 5 mg/mL solution of nc-Si QDs in toluene was then used to spin-cast at a spinning rate of 500 rpm on the top p-Si layer of the solar cells and was dried in vacuum for 2 h.

Characterization Techniques. Micro-Raman scattering measurements were performed to investigate the crystallinity and states of B dopant atoms in SiNWs at room temperature with a 100× objective and a 532 nm excitation light. The excitation power was set at about 0.03 mW to avoid local heating effects caused by the excitation laser. A high-resolution field-emission scanning electron microscope (FESEM, Hitachi S-4800) and transmission electron microscope (TEM, JEOL 2100F) were used for microstructural characterization. Fourier transform infrared (FT-IR) spectral analysis was carried out using an FT-IR spectrometer (Nicolet 4700). The quantum yield of the nanocrystals in toluene solution was measured using the Absolute Quantum Yield Measurement system (model no. SP2150i). Fluorescence spectra of the nc-Si QDs in toluene were measured using a fluorescence spectrophotometer (Jasco FP-8500). Photoluminescence lifetime measurements were carried out by time-correlated single photon counting (TCSPC) using a Horiba Jobin Yvon Fluorocube. UV−vis-NIR reflectance spectra were recorded in the wavelength range of 220−2000 nm using a UV−vis-NIR spectrophotometer (Jasco V-570). *I*−*V* measurements were performed using a Keithley 2400 source meter under illumination with a 1 sun air mass (AM) 1.5 G xenon lamp solar simulator, calibrated using a single-crystalline silicon solar cell (BS-500) provided by Sharp. The cells were illuminated through a 0.25 cm^2 opaque aperture to define the active area and an optical mask supplied by Bunkoukeiki was used to ensure that only the NWs area of the sample was illuminated. The external quantum efficiency (EQE) was measured using a Bunkoukeiki BQE-100F at room temperature to investigate the spectral response of solar cells. The irradiation intensity of the lamp was calibrated using a single-crystalline silicon photodiode (S1337-1010BQ) provided by Hamamatsu Photonics. The band structure of the samples was characterized by XPS (PHI Quantera SXM, ULVAC-PHI) using monochromated Al Kα X-rays with a photon energy of 55 eV for multiplex spectra.

Conflict of Interest: The authors declare no competing financial interest.

Acknowledgment. This work was supported in part by the Funding Program for Next Generation World-Leading Researchers (the NEXT Program), JSPS Kakenhi Grant numbers 26600049 and 26246021 and the World Premier International Research Center Initiative (WPI Initiative), MEXT, Japan. We also thank Dr. Tanaka for carrying out the XPS measurements.

Supporting Information Available: Si 2p XPS spectrum of the components of the hybrid solar cell; band alignment at the interface of p-Si layer and nc-Si QDs; EDS spectrum of nc-Si QDs. The Supporting Information is available free of charge on the ACS Publications website at DOI: 10.1021/acsnano.5b03268.

REFERENCES AND NOTES

1. Kelzenberg, M. D.; Boettcher, S. W.; Petykiewicz, J. A.; Turner-Evans, D. B.; Putnam, M. C.; Warren, E. L.; Spurgeon, J. M.; Briggs, R. M.; Lewis, N. S.; Atwater, H. A. Enhanced Absorption and Carrier Collection in Si Wire Arrays for Photovoltaic Applications. *Nat. Mater.* **2010**, *9*, 239–244.
2. Tian, B.; Zheng, X.; Kempa, T. J.; Fang, Y.; Yu, N.; Yu, G.; Huang, J.; Lieber, C. M. Coaxial Silicon Nanowires as Solar Cells and Nanoelectronic Power Sources. *Nature* **2007**, *449*, 885–890.
3. Peng, K.-Q.; Lee, S.-T. Silicon Nanowires for Photovoltaic Solar Energy Conversion. *Adv. Mater.* **2011**, *23*, 198–215.
4. Hochbaum, A. I.; Chen, R.; Delgado, R. D.; Liang, W.; Garnett, E. C.; Najarian, M.; Majumdar, A.; Yang, P. Enhanced Thermoelectric Performance of Rough Silicon Nanowires. *Nature* **2008**, *451*, 163–168.
5. Kim, D. R.; Lee, C. H.; Rao, P. M.; Cho, I. S.; Zheng, X. Hybrid Si Microwire and Planar Solar Cells: Passivation and Characterization. *Nano Lett.* **2011**, *11*, 2704–2708.
6. Lu, Y.; Lal, A. High-Efficiency Ordered Silicon Nano-Conical-Frustum Array Solar Cells by Self-Powered Parallel Electron Lithography. *Nano Lett.* **2010**, *10*, 4651–4656.
7. Garnett, E. C.; Yang, P. Silicon Nanowire Radial p−n Junction Solar Cells. *J. Am. Chem. Soc.* **2008**, *130*, 9224–9225.
8. Kelzenberg, M. D.; Turner-Evans, D. B.; Kayes, B. M.; Filler, M. A.; Putnam, M. C.; Lewis, N. S.; Atwater, H. A. Single-Nanowire Si Solar Cells. *Proceedings of the 33rd IEEE Photovoltaic Specialists Conference*, San Diego, CA, May 11−16 **2008**; pp 1−6.
9. Yu, Z.; Raman, A.; Fan, S. Fundamental Limit of Nanophotonic Light Trapping in Solar Cells. *Proc. Natl. Acad. Sci. U. S. A.* **2010**, *107*, 17491–17496.
10. Kelzenberg, M. D.; Turner-Evans, D. B.; Putnam, M. C.; Boettcher, S. W.; Briggs, R. M.; Baek, J. Y.; Lewis, N. S.; Atwater, H. A. High-Performance Si Microwire Photovoltaics. *Energy Environ. Sci.* **2011**, *4*, 866–871.
11. Dutta, M.; Fukata, N. Low-temperature UV Ozone-Treated High Efficiency Radial p-n Junction Solar Cells: n-Si NW Arrays Embedded in a p-Si Matrix. *Nano Energy* **2015**, *11*, 219–225.
12. Dutta, M.; Fukata, N. Effect of Shell Growth and Doping Conditions of Core−Shell Homojunction Si Nanowire Solar Cells. *J. Nanosci. Nanotechnol.* **2015**, *15*, 4339–4346.
13. Sato, K.; Dutta, M.; Fukata, N. Inorganic/Organic Hybrid Solar Cells: Optimal Carrier Transport in Vertically Aligned Silicon Nanowire Arrays. *Nanoscale* **2014**, *6*, 6092–6101.
14. Lu, S.; Madhukar, A. Nonradiative Resonant Excitation Transfer from Nanocrystal Quantum Dots to Adjacent Quantum Channels. *Nano Lett.* **2007**, *7*, 3443–3451.
15. Nguyen, H. M.; Seitz, O.; Aureau, D.; Sra, A.; Nijem, N.; Gartstein, Yu. N.; Chabal, Y. J.; Malko, A. V. Spectroscopic Evidence for Nonradiative Energy Transfer Between Colloidal CdSe/ZnS Nanocrystals and Functionalized Silicon Substrates. *Appl. Phys. Lett.* **2011**, *98*, 161904.

16. Chanyawadee, S.; Harley, R. T.; Henini, M.; Talapin, D. V.; Lagoudakis, P. G. Photocurrent Enhancement in Hybrid Nanocrystal Quantum-Dot p-i-n Photovoltaic Devices. *Phys. Rev. Lett.* **2009**, *102*, 077402.
17. Allan, G.; Delerue, C. Energy Transfer Between Semiconductor Nanocrystals: Validity of Förster's Theory. *Phys. Rev. B: Condens. Matter Mater. Phys.* **2007**, *75*, 195311.
18. Lu, S.; Lingley, Z.; Asano, T.; Harris, D.; Barwicz, T.; Guha, S.; Madhukar, A. Photocurrent Induced by Nonradiative Energy Transfer from Nanocrystal Quantum Dots to Adjacent Silicon Nanowire Conducting Channels: Toward a New Solar Cell Paradigm. *Nano Lett.* **2009**, *9*, 4548–4552.
19. Nguyen, H. M.; Seitz, O.; Peng, W.; Gartstein, Y. N.; Chabal, Y. J.; Malko, A. V. Efficient Radiative and Nonradiative Energy Transfer from Proximal CdSe/ ZnS Nanocrystals into Silicon Nanomembranes. *ACS Nano* **2012**, *6*, 5574–5582.
20. Seitz, O.; Caillard, L.; Nguyen, H. M.; Chiles, C.; Chabal, Y. J.; Malko, A. V. Optimizing Non-Radiative Energy Transfer in Hybrid Colloidal-Nanocrystal/Silicon Structures by Controlled Nanopillar Architectures for Future Photovoltaic cells. *Appl. Phys. Lett.* **2012**, *100*, 021902.
21. Achermann, M.; Petruska, M. A.; Kos, S.; Smith, D. L.; Koleske, D. D.; Klimov, V. I. Energy-Transfer Pumping of Semiconductor Nanocrystals Using an Epitaxial Quantum Well. *Nature* **2004**, *429*, 642.
22. Blumstengel, S.; Sadofev, S.; Xu, C.; Puls, J.; Henneberger, F. Converting Wannier into Frenkel Excitons in an Inorganic/ Organic Hybrid Semiconductor Nanostructure. *Phys. Rev. Lett.* **2006**, *97*, 237401.
23. Heliotis, G.; Itskos, G.; Murray, R.; Dawson, M. D.; Watson, I. M.; Bradley, D. D. C. Hybrid Inorganic/Organic Semiconductor Heterostructures with Efficient Non-Radiative Energy Transfer. *Adv. Mater.* **2006**, *18*, 334–338.
24. Veinot, J. G. C. Synthesis, Surface Functionalization, and Properties of Freestanding Silicon Nanocrystals. *Chem. Commun.* **2006**, 4160–4168.
25. Baldwin, R. K.; Pettigrew, K. A.; Garno, J. C.; Power, P. P.; Liu, G. Y.; Kauzlarich, S. M. Room Temperature Solution Synthesis of Alkyl-Capped Tetrahedral Shaped Silicon Nanocrystals. *J. Am. Chem. Soc.* **2002**, *124*, 1150–1151.
26. Zhai, Y.; Dasog, M.; Snitynsky, R. B.; Purkait, T. K.; Aghajamali, M.; Hahn, A. H.; Sturdy, C. B.; Lowary, T. L.; Veinot, J. G. C. Water-Soluble Photoluminescent D-Mannose and L-Alanine Functionalized Silicon Nanocrystals and Their Application to Cancer Cell Imaging. *J. Mater. Chem. B* **2014**, *2*, 8427–8433.
27. Shiohara, A.; Hanada, S.; Prabakar, S.; Fujioka, K.; Lim, T. H.; Yamamoto, K.; Northcote, P. T.; Tilley, R. D. Chemical Reactions on Surface Molecules Attached to Silicon Quantum Dots. *J. Am. Chem. Soc.* **2010**, *132*, 248–253.
28. Hessel, C. M.; Henderson, E. J.; Veinot, J. G. C. Hydrogen Silsesquioxane: A Molecular Precursor for Nanocrystalline Si-SiO_2 Composites and Freestanding Hydride-Surface-Terminated Silicon Nanoparticles. *Chem. Mater.* **2006**, *18*, 6139–6146.
29. Hessel, C. M.; Henderson, E. J.; Veinot, J. G. C. An Investigation of the Formation and Growth of Oxide-Embedded Silicon Nanocrystals in Hydrogen Silsesquioxane-Derived Nanocomposites. *J. Phys. Chem. C* **2007**, *111*, 6956–6961.
30. Kelly, J. A.; Veinot, J. G. C. An Investigation into Near-UV Hydrosilylation of Freestanding Silicon Nanocrystals. *ACS Nano* **2010**, *4*, 4645–4656.
31. Henderson, E. J.; Shuhendler, A. J.; Prasad, P.; Baumann, V.; Maier-Flaig, F.; Faulkner, D. O.; Lemmer, U.; Wu, X. Y.; Ozin, G. A. Colloidally Stable Silicon Nanocrystals with Near-Infrared Photoluminescence for Biological Fluorescence Imaging. *Small* **2011**, *7*, 2507–2516.
32. Dasog, M.; Bader, K.; Veinot, J. G. C. Influence of Halides on the Optical Properties of Silicon Quantum Dots. *Chem. Mater.* **2015**, *27*, 1153–1156.
33. Purkait, T. K.; Iqbal, M.; Wahl, M. H.; Gottschling, K.; Gonzalez, C. M.; Islam, M. A.; Veinot, J. G. C. Borane-Catalyzed Room-Temperature Hydrosilylation of Alkenes/Alkynes on Silicon Nanocrystal Surfaces. *J. Am. Chem. Soc.* **2014**, *136*, 17914–17917.
34. Fukata, N.; Takiguchi, R.; Ishida, S.; Yokono, S.; Hishita, S.; Murakami, K. Recrystallization and Reactivation of Dopant Atoms in Ion-Implanted Silicon Nanowires. *ACS Nano* **2012**, *6*, 3278–3283.
35. Fukata, N. Impurity Doping in Silicon Nanowires. *Adv. Mater.* **2009**, *21*, 2829–32.
36. Fukata, N.; Ishida, S.; Yokono, S.; Takiguchi, R.; Chen, J.; Sekiguchi, T.; Murakami, K. Segregation Behaviors and Radial Distribution of Dopant Atoms in Silicon Nanowires. *Nano Lett.* **2011**, *11*, 651–656.
37. Fano, U. Effects of Configuration Interaction on Intensities and Phase Shifts. *Phys. Rev.* **1961**, *124*, 1866.
38. Fukata, N.; Chen, J.; Sekiguchi, T.; Okada, N.; Murakami, K.; Tsurui, T.; Ito, S. Doping and Hydrogen Passivation of Boron in Silicon Nanowires Synthesized by Laser Ablation. *Appl. Phys. Lett.* **2006**, *89*, 203109.
39. Fukata, N.; Takiguchi, R.; Ishida, S.; Yokono, S.; Hishita, S.; Murakami, K. Recrystallization and Reactivation of Dopant Atoms in Ion-Implanted Silicon Nanowires. *ACS Nano* **2012**, *6*, 3278–3283.
40. Richter, H.; Wang, Z. P.; Ley, L. The One Phonon Raman Spectrum in Microcrystalline Silicon. *Solid State Commun.* **1981**, *39*, 625–629.
41. Campbell, I. H.; Fauchet, P. M. The Effects of Microcrystal Size and Shape on the One Phonon Raman Spectra of Crystalline Semiconductors. *Solid State Commun.* **1986**, *58*, 739–741.
42. Fukata, N.; Oshima, T.; Murakami, K.; Kizuka, T.; Tsurui, T.; Ito, S. Phonon Confinement Effect of Silicon Nanowires Synthesized by Laser Ablation. *Appl. Phys. Lett.* **2005**, *86*, 213112.
43. Yang, C. S.; Bley, R. A.; Kauzlarich, S. M.; Lee, H. W. H.; Delgado, G. R. Synthesis of Alkyl-Terminated Silicon Nanoclusters by a Solution Route. *J. Am. Chem. Soc.* **1999**, *121*, 5191–5195.
44. Höhlein, I. M. D.; Ang, A.; Sinelnikov, R.; Veinot; Rieger, J. G. C. B. Functionalization of Hydride-Terminated Photoluminescent Silicon Nanocrystals with Organolithium Reagents. *Chem. - Eur. J.* **2015**, *21*, 2755–2758.
45. Rowsell, B. D.; Veinot, J. G. C. Reductive Thermolysis of a Heterocyclic Precursor: a Convenient Method for Preparing Luminescent, Surfactant-Stabilized Silicon Nanoparticles. *Nanotechnology* **2005**, *16*, 732–736.
46. Jurbergs, D.; Rogojina, E.; Mangolini, L.; Kortshagen, U. Silicon Nanocrystals with Ensemble Quantum Yields Exceeding 60%. *Appl. Phys. Lett.* **2006**, *88*, 233116.
47. Erogbogbo, F.; Yong, K.-T.; Roy, I.; Xu, G.; Prasad, P. N.; Swihart, M. T. Biocompatible Luminescent Silicon Quantum Dots for Imaging of Cancer Cells. *ACS Nano* **2008**, *2*, 873–878.
48. Takagahara, T.; Takeda, K. Theory of Quantum Confinement Effect on Excitons in Quantum Dots of Indirect-Gap Materials. *Phys. Rev. B: Condens. Matter Mater. Phys.* **1992**, *46*, 15578–15581.
49. Klimov, V. I.; Schwarz, C. J.; McBranch, D. W.; White, C. W. Innitial Carrier Relaxation Dynamics in Ion Implanted Si Nanocrystals: Femtosecond Transient Absorption Study. *Appl. Phys. Lett.* **1998**, *73*, 2603–2605.
50. Dohnalová, K.; Gregorkiewicz, T.; Kusová, K. Silicon Quantum Dots: Surface Matters. *J. Phys.: Condens. Matter* **2014**, *26*, 173201.
51. Yoshida, T.; Sakai, M.; Tanabe, T. *In-situ* Optical Reflection Measurement of a Si(100) Surface under Hydrogen Ion Irradiation. *Mater. Trans.* **2004**, *45*, 2018–2022.
52. Wagner, J. Photoluminescence and Excitation Spectroscopy in Heavily Doped n- and p-Type Silicon. *Phys. Rev. B: Condens. Matter Mater. Phys.* **1984**, *29*, 2002.
53. Schmid, P. E. Optical Absorption in Heavily Doped Silicon. *Phys. Rev. B: Condens. Matter Mater. Phys.* **1981**, *23*, 5531.
54. Streetman, B.; Banerjee, S. K. *Solid State Electronic Devices*; Prentice-Hall: Upper Saddle River, NJ, 2006.
55. Aberle, A. G. *Crystalline Silicon Solar Cell: Advanced Surface Passivation and Analysis*; Centre for Photovoltaic Engineering: University of New South Wales, 1999.

56. Mishima, T.; Taguchi, M.; Sakata, H.; Maruyama, E. Development Status of High Efficiency HIT Solar Cells. *Sol. Energy Mater. Sol. Cells* **2011**, *95*, 18–21.
57. Xu, S.; Huang, S. Y.; Levchenko, I.; Zhou, H. P.; Wei, D. Y.; Xiao, S. Q.; Xu, L. X.; Yan, W. S.; Ostrikov, K. Highly Efficient Silicon Nanoarray Solar Cells by a Single-Step Plasma-Based Process. *Adv. Energy Mater.* **2011**, *1*, 373–376.
58. Zhu, J.; Hsu, C.-M.; Yu, Z.; Fan, S.; Cui, Y. Nanodome Solar Cells with Efficient Light Management and Self-Cleaning. *Nano Lett.* **2010**, *10*, 1979–1984.
59. Zhao, N.; Osedach, T. P.; Chang, L.-Y.; Geyer, S. M.; Wanger, D.; Binda, M. T.; Arango, A. C.; Bawendi, M. G.; Bulovic, V. Colloidal PbS Quantum Dot Solar Cells with High Fill Factor. *ACS Nano* **2010**, *4*, 3743–3752.
60. Stavola, M.; Dexter, D. L.; Knox, R. S. Electron-Hole Pair Excitation in Semiconductors *via* Energy Transfer from an External Sensitizer. *Phys. Rev. B: Condens. Matter Mater. Phys.* **1985**, *31*, 2277–2289.
61. Gupta, A.; Swihart, M. T.; Wiggers, H. Luminescent Colloidal Dispersion of Silicon Quantum Dots from Microwave Plasma Synthesis: Exploring the Photoluminescence Behavior Across the Visible Spectrum. *Adv. Funct. Mater.* **2009**, *19*, 696–703.
62. Godefroo, S.; Hayne, M.; Jivanescu, M.; Stesmans, A.; Zacharias, M.; Lebedev, O. I.; Van Tendeloo, G.; Moshchalkov, V. V. Classification and Control of the Origin of Photoluminescence from Si Nanocrystalls. *Nat. Nanotechnol.* **2008**, *3*, 174.
63. Dhanolova, K.; Poddubny, A. N.; Prokkofiev, A. A.; Boer, W. D.; Chinnaswamy, P. U.; Paulusse, J. M. J.; Zuilhof, H.; Gregorkiewicz, T. Surface Brightens up Si Quantum Dots: Direct Bandgap-Like Size-Tunable Emission. *Light: Sci. Appl.* **2013**, *2*, e47.
64. Mangolini, L.; Kortshagen, U. Plasma Assited Synthesis of Silicon Nanocrystal Inks. *Adv. Mater.* **2007**, *19*, 2513.
65. Moulé, A. J.; Chang, L.; Thambidurai, C.; Vidu, R.; Stroeve, P. Hybrid Solar Cells: Basic Principles and the Role of Ligands. *J. Mater. Chem.* **2012**, *22*, 2351.